Determination of parton distributions

A. Cooper-Sarkar, A. Glazov, G. Li, J. Grebenyuk, V. Lendermann

1 Extraction of the proton PDFs from a combined fit of H1 and ZEUS inclusive DIS cross sections [1]

1.1 Introduction

The kinematics of lepton hadron scattering is described in terms of the variables Q^2, the invariant mass of the exchanged vector boson, Bjorken x, the fraction of the momentum of the incoming nucleon taken by the struck quark (in the quark-parton model), and y which measures the energy transfer between the lepton and hadron systems. The differential cross-section for the neutral current (NC) process is given in terms of the structure functions by

$$\frac{d^2\sigma(e^\pm p)}{dxdQ^2} = \frac{2\pi\alpha^2}{Q^4 x}\left[Y_+\, F_2(x,Q^2) - y^2\, F_L(x,Q^2) \mp Y_-\, xF_3(x,Q^2)\right],$$

where $Y_\pm = 1 \pm (1-y)^2$. The structure functions F_2 and xF_3 are directly related to quark distributions, and their Q^2 dependence, or scaling violation, is predicted by perturbative QCD. For low x, $x \leq 10^{-2}$, F_2 is sea quark dominated, but its Q^2 evolution is controlled by the gluon contribution, such that HERA data provide crucial information on low-x sea-quark and gluon distributions. At high Q^2, the structure function xF_3 becomes increasingly important, and gives information on valence quark distributions. The charged current (CC) interactions also enable us to separate the flavour of the valence distributions at high-x, since their (LO) cross-sections are given by,

$$\frac{d^2\sigma(e^+ p)}{dxdQ^2} = \frac{G_F^2 M_W^4}{(Q^2+M_W^2)^2 2\pi x} x\left[(\bar{u}+\bar{c}) + (1-y)^2(d+s)\right],$$

$$\frac{d^2\sigma(e^- p)}{dxdQ^2} = \frac{G_F^2 M_W^4}{(Q^2+M_W^2)^2 2\pi x} x\left[(u+c) + (1-y)^2(\bar{d}+\bar{s})\right].$$

Parton Density Function (PDF) determinations are usually obtained in global NLO QCD fits [1–3], which use fixed target DIS data as well as HERA data. In such analyses, the high statistics HERA NC e^+p data have determined the low-x sea and gluon distributions, whereas the fixed target data have determined the valence distributions. Now that high-Q^2 HERA data on NC and CC e^+p and e^-p inclusive double differential cross-sections are available, PDF fits can be made to HERA data alone, since the HERA high Q^2 cross-section data can be used to determine the valence distributions. This has the advantage that it eliminates the need for heavy target corrections, which must be applied to the ν-Fe and μD fixed target data. Furthermore there is no need to assume isospin symmetry, i.e. that d in the proton is the same as u in the neutron, since the d distribution can be obtained directly from CC e^+p data.

The H1 and ZEUS collaborations have both used their data to make PDF fits [3], [4]. Both of these data sets have very small statistical uncertainties, so that the contribution of systematic

[1] Contributing authors: A. Cooper-Sarkar, A. Glazov, G. Li for the H1-ZEUS combination group.

uncertainties becomes dominant and consideration of point to point correlations between systematic uncertainties is essential. The ZEUS analysis takes account of correlated experimental systematic errors by the Offset Method, whereas H1 uses the Hessian method [5]. Whereas the resulting ZEUS and H1 PDFs are compatible, the gluon PDFs have rather different shapes, see Fig 7, and the uncertainty bands spanned by these analyses are comparable to those of the global fits.

It is possible to improve on this situation since ZEUS and H1 are measuring the same physics in the same kinematic region. These data have been combined using a 'theory-free' Hessian fit in which the only assumption is that there is a true value of the cross-section, for each process, at each x, Q^2 point [6]. Thus each experiment has been calibrated to the other. This works well because the sources of systematic uncertainty in each experiment are rather different, such that all the systematic uncertainties are re-evaluated. The resulting correlated systematic uncertainties on each of the combined data points are significantly smaller than the statistical errors. This combined data set has been used as the input to an NLO QCD PDF fit. The consistency of the input data set and its small systematic uncertainties enables us to calculate the experimental uncertainties on the PDFs using the χ^2 tolerance, $\Delta\chi^2 = 1$. This represents a further advantage compared to the global fit analyses where increased tolerances of $\Delta\chi^2 = 50 - 100$ are used to account for data inconsistencies.

For the HERAPDF0.1 fit presented here, the role of correlated systematic uncertainties is no longer crucial since these uncertainties are relatively small. This ensures that similar results are obtained using either Offset or Hessian methods, or by simply combining statistical and systematic uncertainties in quadrature. The χ^2 per degree of freedom for a Hessian fit is $553/562$ and for a quadrature fit it is $428/562$. For our central fit we have chosen to combine the 43 systematic uncertainties which result from the separate ZEUS and H1 data sets in quadrature, and to Offset the 4 sources of uncertainty which result from the combination procedure. The χ^2 per degree of freedom for this fit is $477/562$. This procedure results in the most conservative estimates on the resulting PDFs as illustrated in Fig. 1 which compares the PDFs and their experimental uncertainties as evaluated by the procedure of our central fit and as evaluated by treating the 47 systematic uncertainties by the Hessian method.

Despite this conservative procedure, the experimental uncertainties on the resulting PDFs are impressively small and a thorough consideration of further uncertainties due to model assumptions is necessary. In Section 1.2 we briefly describe the data combination procedure. In Section 1.3 we describe the NLO QCD analysis and model assumptions. In Section 1.4 we give results. In Section 1.5 we give a summary of the fit results and specifications for release of the HERAPDF0.1 to LHAPDF. In Section 1.6 we investigate the predictions of the HERAPDF0.1 for W and Z cross-sections at the LHC.

1.2 Data Combination

The data combination is based on assumption that the H1 and ZEUS experiments measure the same cross section at the same kinematic points. The systematic uncertainties of the measurements are separated, following the prescription given by the H1 and ZEUS, into point to point correlated sources α_j and uncorrelated systematic uncertainty, which is added to the statistical uncertainty in quadrature to result in total uncorrelated uncertainty σ_i for each bin i. The

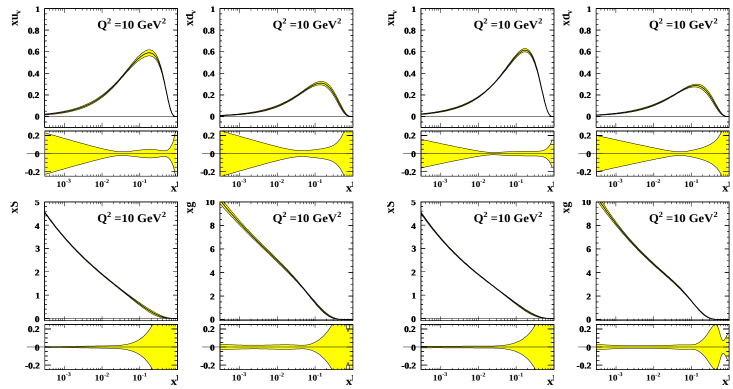

Fig. 1: HERAPDFs, xu_v, xd_v, xS, xg at $Q^2 = 10\text{GeV}^2$. (Left) with experimental uncertainties evaluated as for the central fit (see text) and (right) with experimental uncertainties evaluated by accounting for the 47 systematic errors by the Hessian method.

correlated systematic sources are considered to be uncorrelated between H1 and ZEUS. All uncertainties are treated as multiplicative i.e. proportional to the central values, which is a good approximation for the measurement of the cross sections.

A correlated probability distribution function for the physical cross sections $M^{i,\text{true}}$ and systematic uncertainties $\alpha_{j,\text{true}}$ for a single experiment corresponds to a χ^2 function:

$$\chi^2_{\text{exp}}\left(M^{i,\text{true}}, \alpha_{j,\text{true}}\right) = \sum_i \frac{\left[M^{i,\text{true}} - \left(M^i + \sum_j \frac{\partial M^i}{\partial \alpha_j} \frac{M^{i,\text{true}}}{M^i} (\alpha_{j,\text{true}})\right)\right]^2}{\left(\sigma_i \frac{M^{i,\text{true}}}{M^i}\right)^2} + \sum_j \frac{(\alpha_{j,\text{true}})^2}{\sigma^2_{\alpha_j}}, \tag{1}$$

where M^i are the central values measured by the experiment, $\partial M^i/\partial \alpha_j$ are the sensitivities to the correlated systematic uncertainties and σ_{α_j} are the uncertainties of the systematic sources. For more than one experiment, total χ^2_{tot} can be represented as a sum of χ^2_{exp}. The combination procedure allows to represent χ^2_{tot} in the following form:

$$\begin{aligned}\chi^2_{\text{tot}}\left(M^{i,\text{true}}, \beta_{j,\text{true}}\right) \quad &= \quad \chi^2_0 + \sum_i \frac{\left[M^{i,\text{true}} - \left(M^{i,\text{ave}} + \sum_j \frac{\partial M^{i,\text{ave}}}{\partial \beta_j} \frac{M^{i,\text{true}}}{M^{i,\text{ave}}} (\beta_{j,\text{true}})\right)\right]^2}{\left(\sigma_{i,\text{ave}} \frac{M^{i,\text{true}}}{M^{i,\text{ave}}}\right)^2} \\ &\quad + \sum_j \frac{(\beta_{j,\text{true}})^2}{\sigma^2_{\beta_j}}. \end{aligned} \tag{2}$$

Here the sum runs over a union set of the cross section bins. The value of the χ^2_{tot} at the minimum, χ^2_0, quantifies consistency of the experiments. $M^{i,\text{ave}}$ are the average values of the cross sections and β_j correspond to the new systematic sources which can be obtained from the original sources α_j through the action of an orthogonal matrix. In essence, the average of several data sets allows one to represent the total χ^2 in a form which is similar to that corresponding to a single data set, Eq. 1, but with modified systematic sources.

The combination is applied to NC and CC cross section data taken with e^+ and e^- beams simultaneously to take into account correlation of the systematic uncertainties. The data taken with proton beam energies of $E_p = 820$ GeV and $E_p = 920$ GeV are combined together for inelasticity $y < 0.35$, for this a small center of mass energy correction is applied. For the combined data set there are 596 data points and 43 experimental systematic sources. The $\chi^2_0/dof = 510/599$ is below 1, which indicates conservative estimation of the uncorrelated systematics.

Besides the experimental uncertainties, four additional sources related to the assumptions made for the systematic uncertainties are considered. Two of the extra sources deal with correlation of the H1 and ZEUS data for estimation of the photoproduction background and simulation of hadronic energy scale. These sources introduce additional $\sim 1\%$ uncertainty for $y > 0.6$ and $y < 0.02$ data. The third source covers uncertainty arising from the center of mass correction by varying $F_L = F_L^{QCD}$ to $F_L = 0$. The resulting uncertainty reaches few per mille level for $y \sim 0.35$. Finally, some of the systematic uncertainties, for example background subtraction, may not be necessary multiplicative but rather additive, independent of the cross section central values. The effect of additive assumption for the errors is evaluated by comparing the average obtained using Eq. 1 and an average in which $M^{i,\mathrm{true}}/M^{i,\mathrm{ave}}$ scaling is removed for all but global normalization errors.

1.3 QCD Analysis

The QCD predictions for the structure functions are obtained by solving the DGLAP evolution equations [7–9] at NLO in the $\overline{\mathrm{MS}}$ scheme with the renormalisation and factorization scales chosen to be Q^2 [2]. The DGLAP equations yield the PDFs at all values of Q^2 provided they are input as functions of x at some input scale Q^2_0. This scale has been chosen to be $Q^2_0 = 4\mathrm{GeV}^2$ and variation of this choice is considered as one of the model uncertainties. The resulting PDFs are then convoluted with NLO coefficient functions to give the structure functions which enter into the expressions for the cross-sections. The choice of the heavy quark masses is, $m_c = 1.4, m_b = 4.75$GeV, and variation of these choices is included in the model uncertainties. For this preliminary analysis, the heavy quark coefficient functions have been calculated in the zero-mass variable flavour number scheme. The strong coupling constant was fixed to $\alpha_s(M_Z^2) = 0.1176$ [12], and variations in this value of ± 0.002 have also been considered.

The fit is made at leading twist. The HERA data have a minimum invariant mass of the hadronic system, W^2, of $W^2_{min} = 300$ GeV^2 and a maximum x, $x_{max} = 0.65$, such that they are in a kinematic region where there is no sensitivity to target mass and large-x higher twist contributions. However a minimum Q^2 cut is imposed to remain in the kinematic region where perturbative QCD should be applicable. This has been chosen to be $Q^2_{min} = 3.5$ GeV^2. Variation of this cut is included as one of the model uncertainties.

A further model uncertainty is the choice of the initial parameterization at Q^2_0. Three types of parameterization have been considered. For each of these choices the PDFs are parameterized

[2]The programme QCDNUM [10] has been used and checked against the programme QCDfit [11].

by the generic form

$$xf(x) = Ax^B(1-x)^C(1 + Dx + Ex^2 + Fx^3), \tag{3}$$

and the number of parameters is chosen by 'saturation of the χ^2', such that parameters D, E, F are only varied if this brings significant improvement to the χ^2. Otherwise they are set to zero.

The first parameterization considered follows that used by the ZEUS collaboration. The PDFs for u valence, $xu_v(x)$, d valence, $xd_v(x)$, total sea, $xS(x)$, the gluon, $xg(x)$, and the difference between the d and u contributions to the sea, $x\Delta(x) = x(\bar{d} - \bar{u})$, are parameterized.

$$\begin{aligned}
xu_v(x) &= A_{uv}x^{B_{uv}}(1-x)^{C_{uv}}(1 + D_{uv}x + E_{uv}x^2) \\
xd_v(x) &= A_{dv}x^{B_{dv}}(1-x)^{C_{dv}} \\
xS(x) &= A_S x^{B_S}(1-x)^{C_S} \\
xg(x) &= A_g x^{B_g}(1-x)^{C_g}(1 + D_g x) \\
x\Delta(x) &= A_\Delta x^{B_\Delta}(1-x)^{C_\Delta}
\end{aligned}$$

The total sea is given by, $xS = 2x(\bar{u} + \bar{d} + \bar{s} + \bar{c} + \bar{b})$, where $\bar{q} = q_{sea}$ for each flavour, $u = u_v + u_{sea}, d = d_v + d_{sea}$ and $q = q_{sea}$ for all other flavours. There is no information on the shape of the $x\Delta$ distribution in a fit to HERA data alone and so this distribution has its parameters fixed, such that its shape is consistent with Drell-Yan data and its normalization is consistent with the size of the Gottfried sum-rule violation. A suppression of the strange sea with respect to the non-strange sea of a factor of 2 at Q^2_0, is imposed consistent with neutrino induced dimuon data from NuTeV. The normalisation parameters, A_{uv}, A_{dv}, A_g, are constrained to impose the number sum-rules and momentum sum-rule. The B parameters, B_{uv} and B_{dv} are set equal, since there is no information to constrain any difference. Finally this ZEUS-style parameterization has eleven free parameters.

The second parameterization considered follows that of the H1 Collaboration The choice of quark PDFs which are parameterized is different. The quarks are considered as u-type and d-type, $xU = x(u_v + u_{sea} + c)$, $xD = x(d_v + d_{sea} + s)$, $x\bar{U} = x(\bar{u} + \bar{c})$ and $x\bar{D} = x(\bar{d} + \bar{s})$, assuming $q_{sea} = \bar{q}$, as usual. These four (anti-)quark distributions are parameterized separately.

$$\begin{aligned}
xU(x) &= A_U x^{B_U}(1-x)^{C_U}(1 + D_U x + E_U x^2 + F_U x^3) \\
xD(x) &= A_D x^{B_D}(1-x)^{C_D}(1 + D_D x) \\
x\bar{U}(x) &= A_{\bar{U}} x^{B_{\bar{U}}}(1-x)^{C_{\bar{U}}} \\
x\bar{D}(x) &= A_{\bar{D}} x^{B_{\bar{D}}}(1-x)^{C_{\bar{D}}} \\
xg(x) &= A_g x^{B_g}(1-x)^{C_g}
\end{aligned}$$

Since the valence distributions must vanish as $x \to 0$, the parameters, A and B are set equal for xU and $x\bar{U}$; $A_U = A_{\bar{U}}$, $B_U = B_{\bar{U}}$; and for xD and $x\bar{D}$; $A_D = A_{\bar{D}}$, $B_D = B_{\bar{D}}$. Since there is no information on the flavour structure of the sea it is also necessary to set $B_{\bar{U}} = B_{\bar{D}}$, such that there is a single B parameter for all four quark distributions. The normalisation, A_g, of the gluon is determined from the momentum sum-rule and the parameters D_U and D_D are determined by the number sum-rules. Assuming that the strange and charm quark distributions can be expressed as x independent fractions, $f_s = 0.33$ and $f_c = 0.15$, of the d and u type sea respectively, gives the further constraint $A_{\bar{U}} = A_{\bar{D}}(1 - f_s)/(1 - f_c)$, which ensures that $\bar{u} = \bar{d}$ at low x. Finally this H1-style parameterization has 10 free parameters.

The third parameterization we have considered combines the best features of the previous two. It has less model dependence than the ZEUS-style parameterization in that it makes fewer assumptions on the form of sea quark asymmetry $x\Delta$, and it has less model dependence than the H1-style parameterization in that it does not assume equality of all B parameters. Furthermore, although all types of parameterization give acceptable χ^2 values, the third parameterization has the best χ^2 and it gives the most conservative experimental errors. This is the parameterization which we chose for our central fit. The PDFs which are parameterized are xu_v, xd_v, xg and $x\bar{U}$, $x\bar{D}$.

$$xu_v(x) = A_{uv} x^{B_{uv}} (1 - x)^{C_{uv}} (1 + D_{uv} x + E_{uv} x^2)$$

$$xd_v(x) = A_{dv} x^{B_{dv}} (1 - x)^{C_{dv}}$$

$$x\bar{U}(x) = A_{\bar{U}} x^{B_{\bar{U}}} (1 - x)^{C_{\bar{U}}}$$

$$x\bar{D}(x) = A_{\bar{D}} x^{B_{\bar{D}}} (1 - x)^{C_{\bar{D}}}$$

$$xg(x) = A_g x^{B_g} (1 - x)^{C_g}$$

The normalisation parameters, A_{uv}, A_{dv}, A_g, are constrained to impose the number sum-rules and momentum sum-rule. The B parameters, B_{uv} and B_{dv} are set equal, $B_{uv} = B_{dv}$ and the B parameters $B_{\bar{U}}$ and $B_{\bar{D}}$ are also set equal, $B_{\bar{U}} = B_{\bar{D}}$, such that there is a single B parameter for the valence and another different single B parameter for the sea distributions. Assuming that the strange and charm quark distributions can be expressed as x independent fractions, $f_s = 0.33$ and $f_c = 0.15$, of the d and u type sea, gives the further constraint $A_{\bar{U}} = A_{\bar{D}}(1 - f_s)/(1 - f_c)$. The value of $f_s = 0.33$ has been chosen to be consistent with determinations of this fraction using neutrino induced di-muon production. This value has been varied to evaluate model uncertainties. The charm fraction has been set to be consistent with dynamic generation of charm from the start point of $Q^2 = m_c^2$, in a zero-mass-variable-flavour-number scheme. A small variation of the value of f_c is included in the model uncertainties. Finally this parameterization has 11 free parameters.

It is well known that the choice of parameterization can affect both PDF shapes and the size of the PDF uncertainties. Fig 2 compares the PDFs and their uncertainties as evaluated using these three different parameterizations. As mentioned earlier, the third parameterization results in the most conservative uncertainties.

We present results for the HERA PDFs based on the third type of parameterization, including six sources of model uncertainty as specified in Table 1. We also compare to results obtained by varying $\alpha_s(M_Z^2)$ and by varying the choice of parameterization to those of the ZEUS and the H1 styles of parameterization.

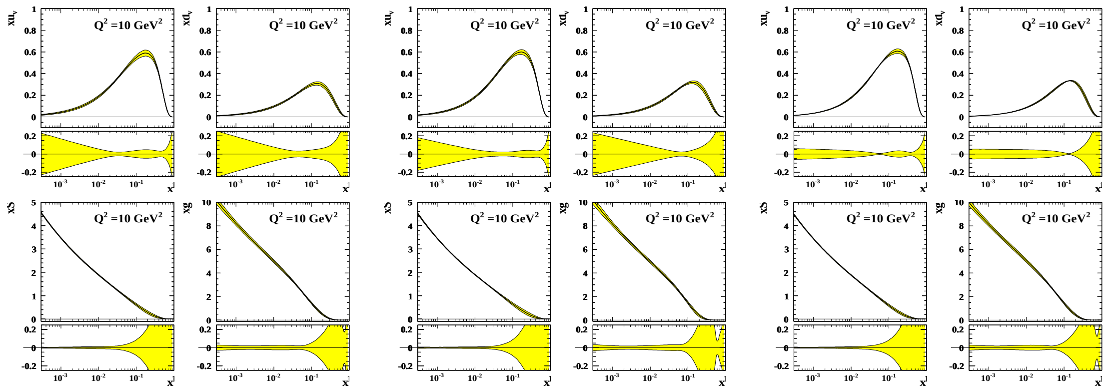

Fig. 2: HERAPDFs, xu_v, xd_v, xS, xg and their uncertainties at $Q^2 = 10\text{GeV}^2$. (Left) for the central fit; (centre) for the ZEUS-style parameterization; (right) for the H1-style parameterization

Model variation	Standard value	Upper Limit	Lower limit
m_c	1.4	1.35	1.5
m_b	4.75	4.3	5.0
Q^2_{min}	3.5	2.5	5.0
Q^2_0	4.0	2.0	6.0
f_s	0.33	0.25	0.40
f_c	0.15	0.12	0.18

Table 1: Standard values of input parameters and cuts, and the variations considered to evaluate model uncertainty

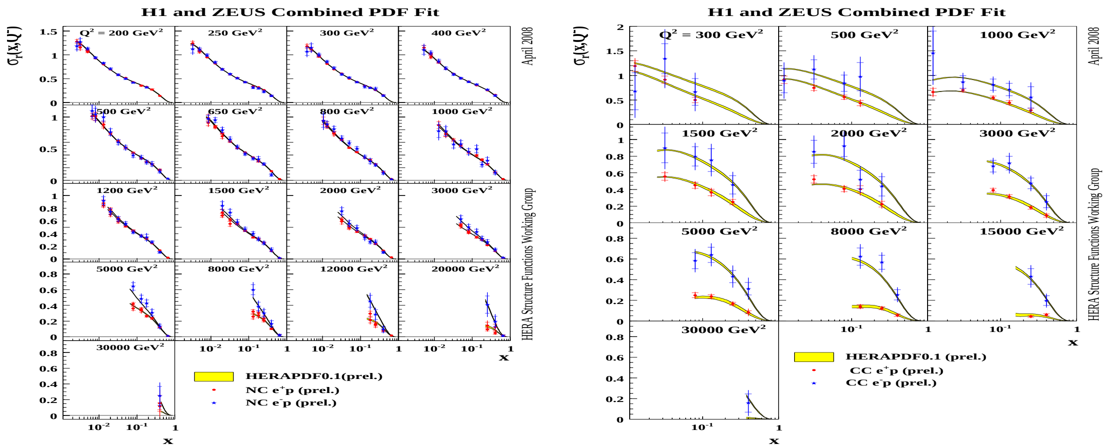

Fig. 3: HERA combined NC (left) and CC (right) data. The predictions of the HERAPDF0.1 fit are superimposed. The uncertainty bands illustrated derive from both experimental and model sources

1.4 Results

In Fig. 3 we show the HERAPDF0.1 superimposed on the combined data set for NC data and CC data. In Fig 4 we show the NC data at low Q^2, and we illustrate scaling violation by showing the reduced cross-section vs. Q^2 for a few representative x bins. The predictions of the HERAPDF0.1 fit are superimposed, together with the predictions of the ZEUS-JETS and H1PDF2000 PDFs.

Fig. 5 shows the HERAPDF0.1 PDFs, xu_v, xd_v, xS, xg, as a function of x at the starting scale $Q^2 = 4$ GeV^2 and at $Q^2 = 10$ GeV^2. Fig. 6 shows the same PDFs at the scales $Q^2 = 100, 10000$ GeV^2. Fractional uncertainty bands are shown beneath each PDF. The experimental and model uncertainties are shown separately. As the PDFs evolve with Q^2 the total uncertainty becomes impressively small.

The total uncertainty of the PDFs obtained from the HERA combined data set is much reduced compared to the PDFs extracted from the analyses of the separate H1 and ZEUS data sets, as can be seen from the summary plot Fig. 7, where these new HERAPDF0.1 PDFs are compared to the ZEUS-JETS and H1PDF2000 PDFs. It is also interesting to compare the present HERAPDF0.1 analysis of the combined HERA-I data set with an analysis of the separate data sets which uses the same parameterization and assumptions. Fig 8 makes this comparison. It is clear that it is the data combination, and not the choice of parameterization and assumptions, which has resulted in reduced uncertainties for the low-x gluon and sea PDFs.

The break-up of the HERAPDFs into different flavours is illustrated in Fig. 9, where the PDFs xU, xD, $x\bar{U}$, $x\bar{D}$ and $x\bar{u}, x\bar{d}, x\bar{c}, x\bar{s}$ are shown at $Q^2 = 10$ GeV^2. The model uncertainty on these PDFs from variation of Q^2_{min}, Q^2_0, m_c and m_b is modest. The model uncertainty from variation of f_s and f_c is also modest except for its obvious effect on the charm and strange quark distributions.

It is also interesting to look at the results obtained from using the ZEUS-style and H1

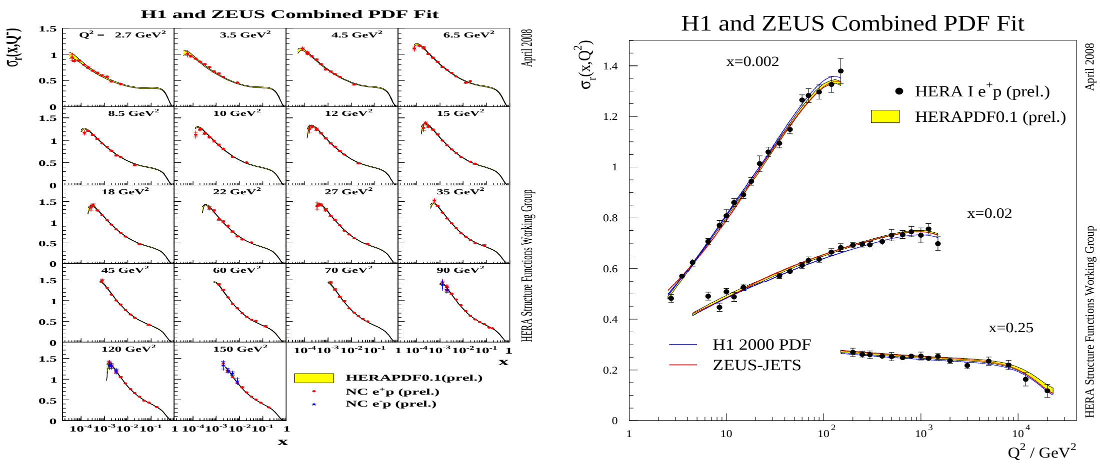

Fig. 4: Left: HERA combined NC data at low Q^2. Right: the NC reduced cross-section vs Q^2 for three x-bins. The predictions of the HERAPDF0.1 fit are superimposed, together with the predictions of the ZEUS-JETS and H1PDF2000 PDFs

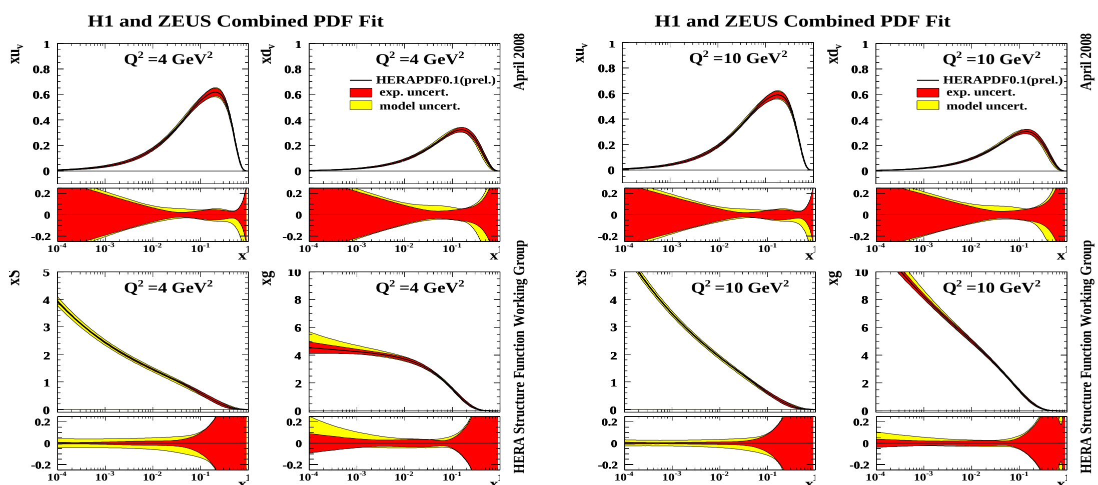

Fig. 5: HERAPDFs, xu_v, xd_v, xS, xg, at (left) $Q^2 = 4$ GeV^2 and (right) $Q^2 = 10$ GeV^2. Fractional uncertainty bands are shown beneath each PDF. The experimental and model uncertainties are shown separately as the red and yellow bands respectively

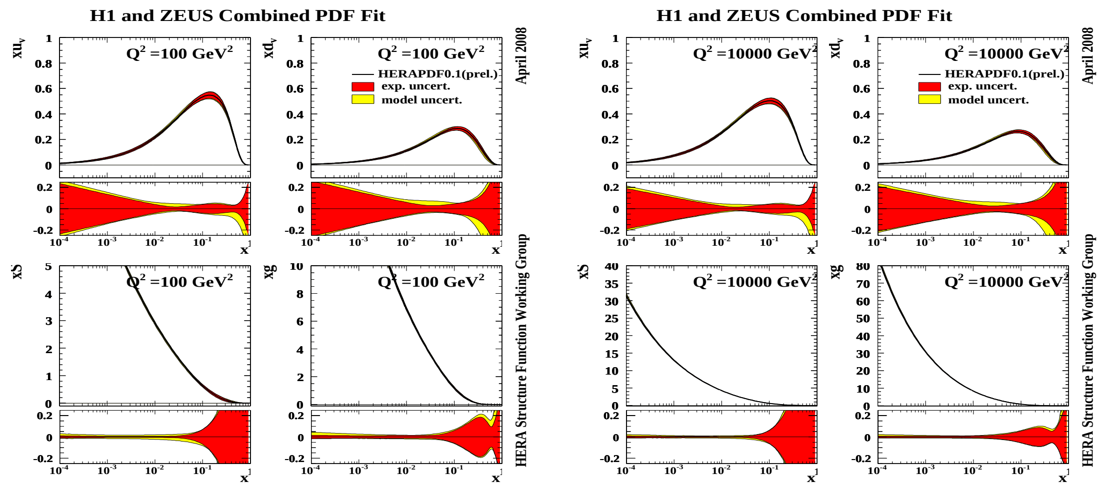

Fig. 6: HERAPDFs, xu_v, xd_v, xS, xg, at (left) $Q^2 = 100$ GeV^2 and (right) $Q^2 = 10000$ GeV^2. Fractional uncertainty bands are shown beneath each PDF. The experimental and model uncertainties are shown separately as the red and yellow bands respectively

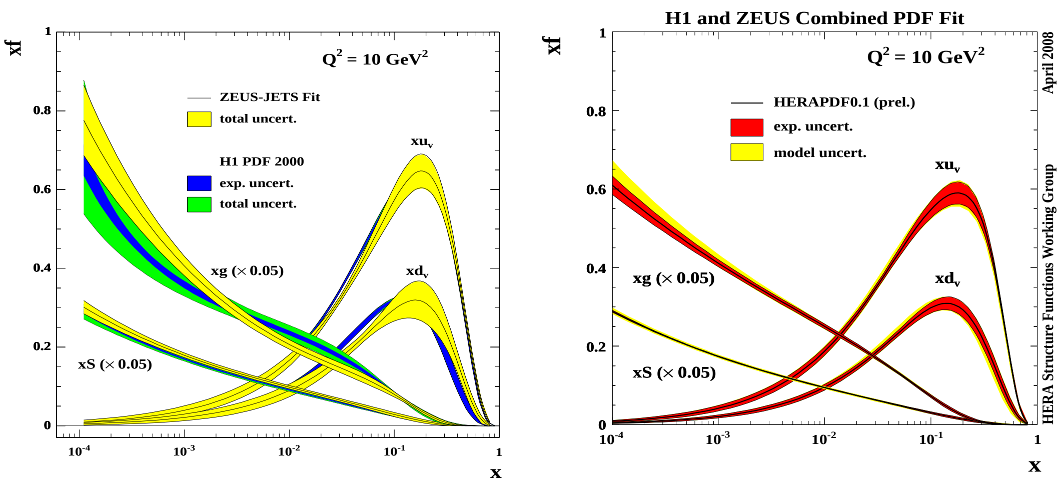

Fig. 7: Left: PDFs from the ZEUS-JETS and H1PDF2000 PDF separate analyses of ZEUS and H1. Right: HERAPDF0.1 PDFs from the analysis of the combined data set

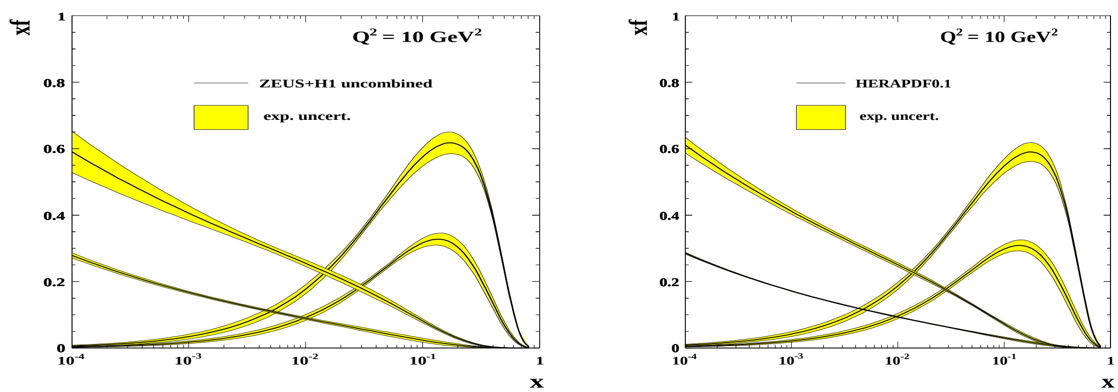

Fig. 8: Left: PDFs resulting from an analysis of the H1 and ZEUS separate data sets using the same parameterization and assumptions as HERAPDF0.1. Right: HERAPDF0.1 PDFs from the analysis of the combined data set (experimental uncertainties only)

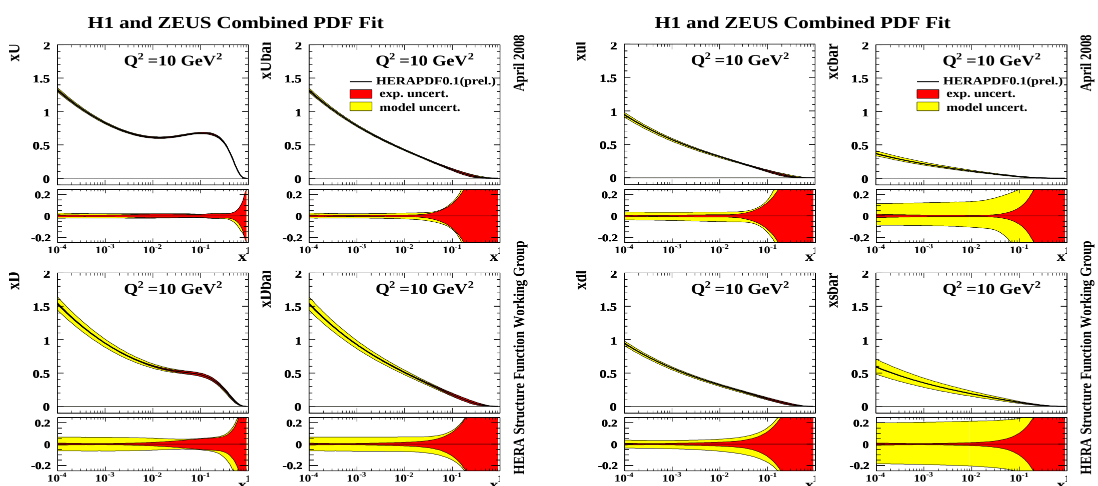

Fig. 9: HERAPDFs at $Q^2 = 10\mathrm{GeV}^2$: (left) $xU, xD, x\bar{U}, x\bar{D}$; (right) $x\bar{u}, x\bar{d}, x\bar{c}, x\bar{s}$. Fractional uncertainty bands are shown beneath each PDF. The experimental and model uncertainties are shown separately as the red and yellow bands respectively

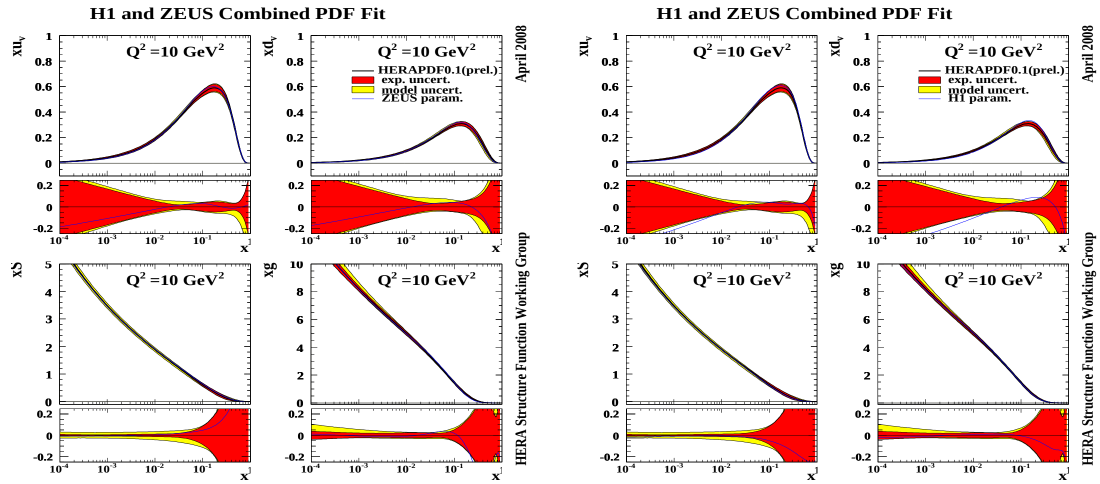

Fig. 10: HERAPDFs at $Q^2 = 10\mathrm{GeV}^2$: with the results for the ZEUS-style parameterization (left) and for the H1-style parameterization (right) superimposed as a blue line.

style parameterizations described in Section 1.3. In Fig. 10 these alternative parameterizations are shown as a blue line superimposed on the HERAPDF0.1 PDFs. These variations in parameterization produce changes in the resulting PDFs which are comparable to the experimental uncertainties in the measured kinematic range. A further variation of parameterization originates from the fact that, if the D parameter for the gluon is allowed to be non-zero, then each type of parameterization yields a double minimum in χ^2 such that the gluon may take a smooth or a 'humpy' shape. Although the lower χ^2 is obtained for the for the smooth shape, the χ^2 for the 'humpy' shape is still acceptable. The PDFs for the 'humpy' version of our chosen form of parameterization are compared to the standard version in Fig. 11, where they are shown as a blue line superimposed on the HERAPDF0.1 PDFs. This comparison is shown at $Q^2 = 4\mathrm{GeV}^2$, where the difference is the greatest. Nevertheless the resulting PDFs are comparable to those of the standard choice. This explains a long-standing disagreement in the shape of the gluon obtained by the separate ZEUS-JETS and H1PDF200 analyses. The ZEUS data favoured the smooth shape and the H1 data favoured the 'humpy' shape. However the precision of the combined data set results in PDFs for these shapes which are not significantly different in the measured kinematic region.

It is also interesting to compare the PDFs for the standard choice to those obtained with a different input value of $\alpha_s(M_Z^2)$. The uncertainty on the current PDG value of $\alpha_s(M_Z^2)$ is ± 0.002 and thus we vary our central choice by this amount. The results are shown in Fig. 12, where we can see that this variation only affects the gluon PDF, such that the larger(smaller) value of $\alpha_s(M_Z^2)$ results in a harder(softer) gluon as predicted by the DGLAP equations. The change is outside total uncertainty bands of the standard fit. Finally, Figs. 13 and 14 compare the HERAPDF0.1 PDFs to those of the CTEQ and the MRST/MSTW groups respectively. The uncertainty bands of the CTEQ and MRST/MSTW analyses have been scaled to represent 68% CL limits for direct comparability to the HERAPDF0.1. The HERAPDF0.1 analysis has much

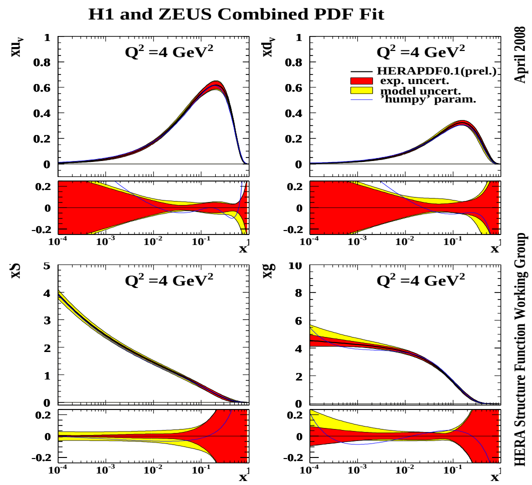

Fig. 11: HERAPDFs at $Q^2 = 4\mathrm{GeV}^2$: with the results for the humpy version superimposed as a blue line.

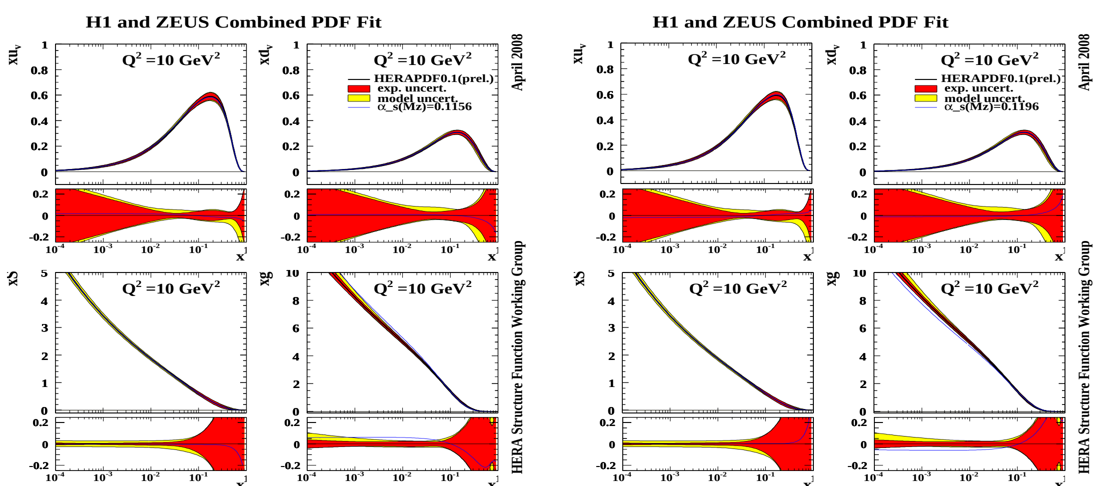

Fig. 12: HERAPDFs at $Q^2 = 10\mathrm{GeV}^2$: with the results for $\alpha_s(M_Z^2) = 0.1156$ (left) and for $\alpha_s(M_Z^2) = 0.1196$ (right) superimposed as a blue line.

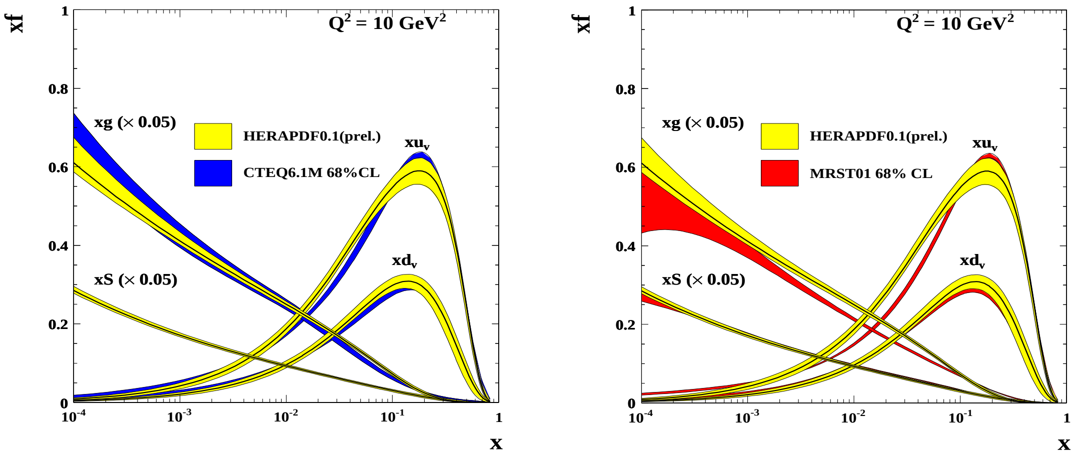

Fig. 13: HERAPDFs at $Q^2 = 10\text{GeV}^2$ compared to the PDFs from CTEQ6.1 and MRST01

improved precision on the low-x gluon.

1.5 Summary of HERAPDF0.1 results

Now that high-Q^2 HERA data on NC and CC e^+p and e^-p inclusive double differential cross-sections are available, PDF fits can be made to HERA data alone, since the HERA high Q^2 cross-section data can be used to determine the valence distributions and HERA low Q^2 cross-section data can be used to determine the Sea and gluon distributions. The combined HERA-I data set, of neutral and charged current inclusive cross-sections for e^+p and e^-p scattering, has been used as the sole input for an NLO QCD PDF fit in the DGLAP formalism. The consistent treatment of systematic uncertainties in the joint data set ensures that experimental uncertainties on the PDFs can be calculated without need for an increased χ^2 tolerance. This results in PDFs with greatly reduced experimental uncertainties compared to the separate analyses of the ZEUS and H1 experiments. Model uncertainties, including those arising from parameterization dependence, have also been carefully considered. The resulting HERAPDFs (called HERAPDF0.1) have improved precision at low-x compared to the global fits. this will be important for predictions of the W and Z cross-sections at the LHC, as explored in the next Section.

These PDFs have been released on LHAPDF in version LHAPDF.5.6: they consist of a central value and 22 experimental eigenvectors plus 12 model alternatives. The user should sum over Nmem=1,22 for experimental uncertainties and over Nmem=1,34 for total uncertainties.

1.6 Predictions for W and Z cross-sections at the LHC using the HERAPDF0.1

At leading order (LO), W and Z production occur by the process, $q\bar{q} \rightarrow W/Z$, and the momentum fractions of the partons participating in this subprocess are given by, $x_{1,2} = \frac{M}{\sqrt{s}} exp(\pm y)$, where M is the centre of mass energy of the subprocess, $M = M_W$ or M_Z, $\sqrt{s}$ is the centre of mass energy of the reaction ($\sqrt{s} = 14$ TeV at the LHC) and $y = \frac{1}{2} ln \frac{(E+pl)}{(E-pl)}$ gives the parton

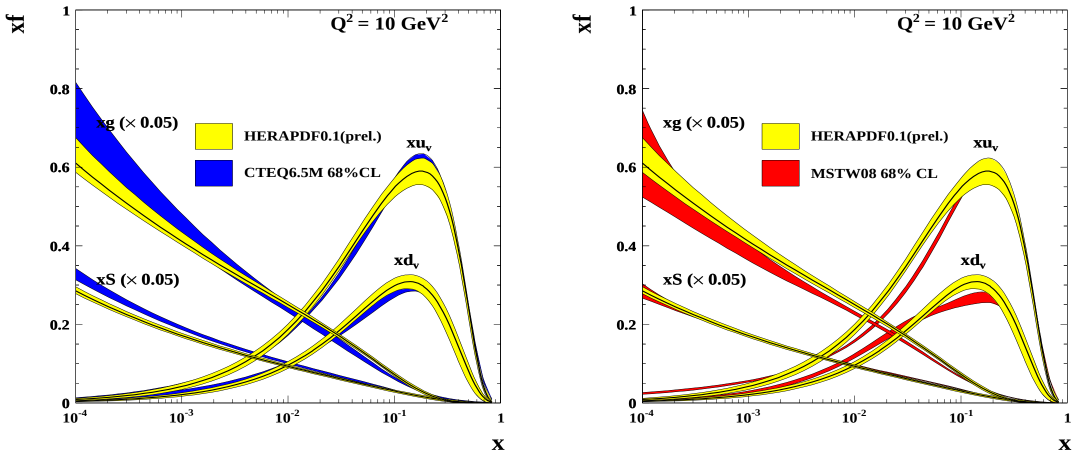

Fig. 14: HERAPDFs at $Q^2 = 10\mathrm{GeV}^2$ compared to the PDFs from CTEQ6.5 and MSTW08(prel.)

rapidity. The kinematic plane for LHC parton kinematics is shown in Fig. 15. Thus, at central rapidity, the participating partons have small momentum fractions, $x \sim 0.005$. Moving away from central rapidity sends one parton to lower x and one to higher x, but over the central rapidity range, $|y| < 2.5$, x values remain in the range, $5 \times 10^{-4} < x < 5 \times 10^{-2}$. Thus, in contrast to the situation at the Tevatron, the scattering is happening mainly between sea quarks. Furthermore, the high scale of the process $Q^2 = M^2 \sim 10,000$ GeV^2 ensures that the gluon is the dominant parton, see Fig. 15, so that these sea quarks have mostly been generated by the flavour blind $g \to q\bar{q}$ splitting process. Thus the precision of our knowledge of W and Z cross-sections at the LHC is crucially dependent on the uncertainty on the momentum distribution of the low-x gluon.

HERA data have already dramatically improved our knowledge of the low-x gluon, as discussed in earlier proceedings of the HERALHC workshop [13]. Now that the precision of HERA data at small-x have been dramatically improved by the combination of H1 and ZEUS HERA-I data, we re-investigate the consequences for predictions of W, Z production at the LHC.

Predictions for the W/Z cross-sections, decaying to the lepton decay mode, using CTEQ, ZEUS PDFs and the HERAPDF0.1 are summarised in Table 2. Note that the uncertainties of CTEQ PDFS have been rescaled to represent 68% CL, in order to be comparable to the HERA PDF uncertainties. The precision on the predictions of the global fits (CTEQ6.1/5 and ZEUS-2002) for the total W/Z cross-sections is $\sim 3\%$ at 68% CL. The precision of the ZEUS-2005 PDF fit prediction, which used only ZEUS data, is comparable, since information on the low-x gluon is coming from HERA data alone. The increased precision of the HERAPDF0.1 low-x gluon PDF results in increased precision of the W/Z cross-section predictions of $\sim 1\%$.

It is interesting to consider the predictions as a function of rapidity. Fig 16 shows the predictions for W^+, W^-, Z production as a function of rapidity from the HERAPDF0.1 PDF fit and compares them to the predictions from a PDF fit, using the same parameterization and assumptions, to the H1 and ZEUS data from HERA-I uncombined. The increase precision due

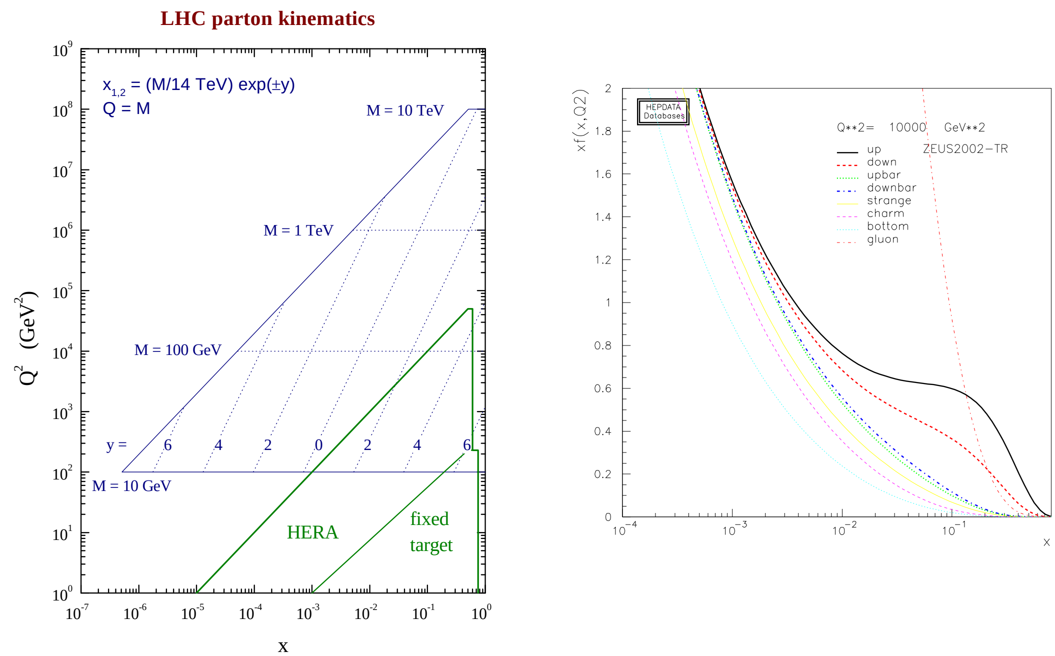

Fig. 15: Left plot: The LHC kinematic plane (thanks to James Stirling). Right plot: Typical PDF distributions at $Q^2 = 10,000$ GeV^2.

to the combination is impressive. Fig. 17 show the predictions for W^+, W^-, Z production as a function of rapidity from the CTEQ6.1, 6.6 and MRST01 PDF fits for comparison. The uncertainties on the CTEQ and MRST PDF predictions have been rescaled to represent 68% CL limits, for direct comparability to the HERAPDF0.1 uncertainties. At central rapidity these limits give an uncertainty on the boson cross-sections of $\sim 5\%$, ($\sim 3\%$),($\sim 2\%$) for CTEQ6.1, (CTEQ6.6), (MRST01) compared to $\sim 1\%$ for the HERAPDF0.1.

So far, only experimental uncertainties have been included in these evaluations. It is also necessary to include model uncertainties. Fig. 18 shows the W^+, W^-, Z rapidity distributions including the six sources of model uncertainty detailed in Section 1.3. These model uncertainties increase the total uncertainty at central rapidity to $\sim 2\%$. Further uncertainty due to the choice of $\alpha_s(M_Z)$ is small because, although a lower (higher) choice results in a larger (smaller) gluon at low x, the rate of QCD evolution is lower (higher) and this largely compensates. Uncertainties due to the choice of parameterization also have little impact on the boson rapidity spectra in the central region as illustrated in Fig. 18 by the superimposed blue line, which represents the alternative 'humpy' gluon parameterization (see Sec. 1.4).

Since the PDF uncertainty feeding into the W^+, W^- and Z production is mostly coming from the gluon PDF, for all three processes, there is a strong correlation in their uncertainties, which can be removed by taking ratios. Figs. 16, 17 and 18 also show the W asymmetry

$$A_W = (W^+ - W^-)/(W^+ + W^-).$$

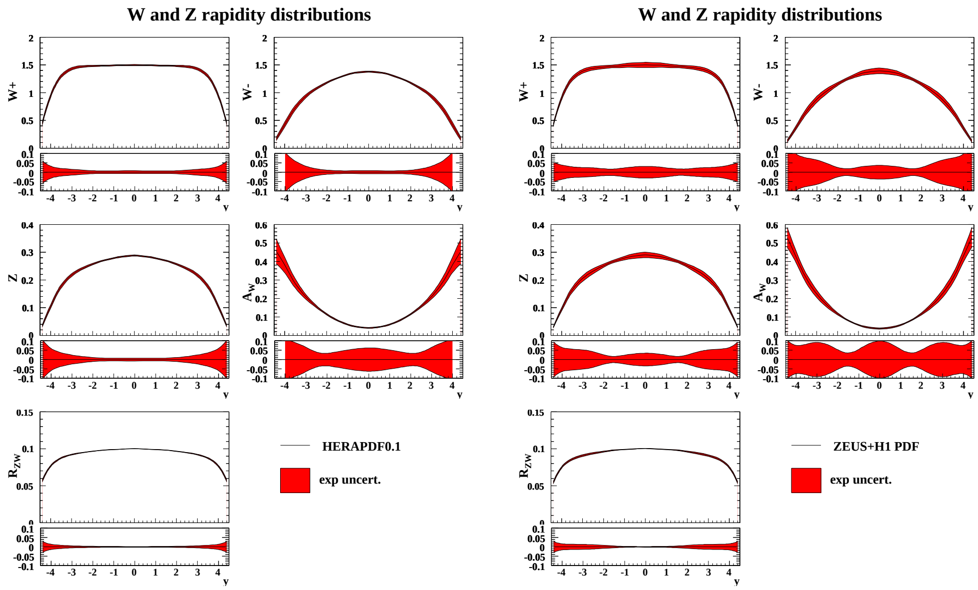

Fig. 16: The W^+, W^-, Z rapidity distributions, A_W and R_{ZW} (see text) and their uncertainties as predicted by (left) HERAPDF0.1 (right) a similar fit to the uncombined ZEUS and H1 data from HERA-I.

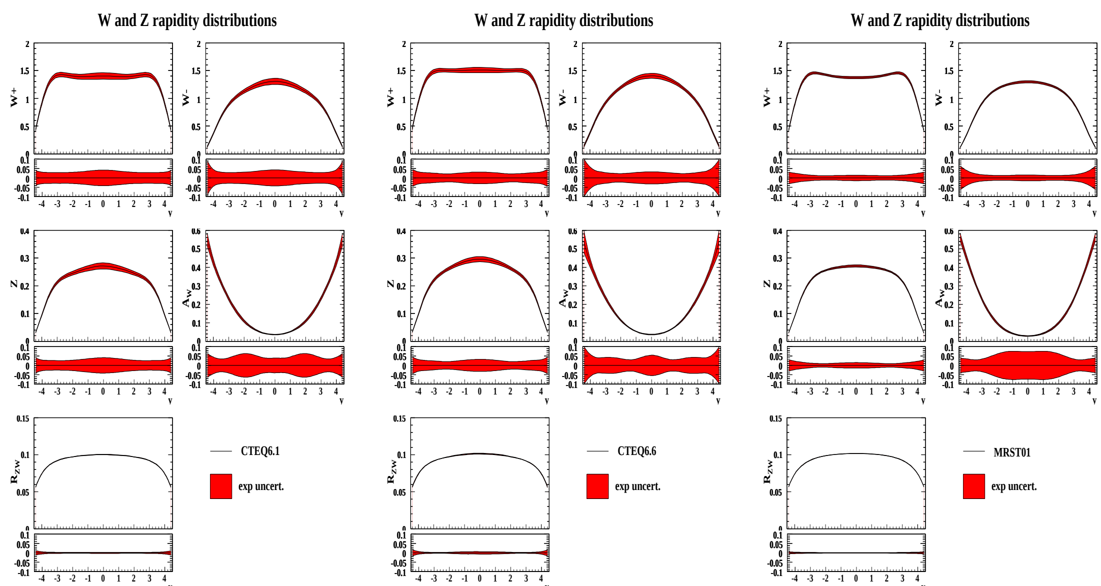

Fig. 17: The W^+, W^-, Z rapidity distributions, A_W and R_{ZW} (see text) and their uncertainties (scaled to 68% CL) as predicted by (left) CTEQ6.1, (middle) CTEQ6.6, right (MRST01

PDF Set	$\sigma(W^+).B(W^+ \to l^+\nu_l)$	$\sigma(W^-).B(W^- \to l^-\bar{\nu}_l)$	$\sigma(Z).B(Z \to l^+l^-)$
CTEQ6.1	11.61 ± 0.34 nb	8.54 ± 0.26 nb	1.89 ± 0.05 nb
CTEQ6.5	12.47 ± 0.28 nb	9.14 ± 0.22 nb	2.03 ± 0.04 nb
ZEUS-2002	12.07 ± 0.41 nb	8.76 ± 0.30 nb	1.89 ± 0.06 nb
ZEUS-2005	11.87 ± 0.45 nb	8.74 ± 0.31 nb	1.97 ± 0.06 nb
HERAPDF0.1	12.14 ± 0.13 nb	9.08 ± 0.14 nb	1.99 ± 0.025 nb

Table 2: LHC W/Z cross-sections for decay via the lepton mode, for various PDFs, with 68% CL uncertainties.

The experimental PDF uncertainty on the asymmetry is larger ($\sim\ 5\%$ for both CTEQ and HERAPDFs, $\sim\ 7\%$ for the MRST01 PDFs) than that on the individual distributions and the variation between PDF sets is also larger - compare the central values of the CTEQ and MRST predictions, which are almost 25% discrepant. This is because the asymmetry is sensitive to the difference in the valence PDFs, $u_v - d_v$, in the low-x region, $5 \times 10^{-4} < x < 5 \times 10^{-2}$, where there is no constraint from current data. To see this consider that at LO,

$$A_W \sim (u\bar{d} - d\bar{u})/(u\bar{d} + d\bar{u} + c\bar{s} + s\bar{c})$$

and that $\bar{d} \sim \bar{u}$ at low-x. (Note that the $c\bar{s}$ and $s\bar{c}$ contributions cancel out in the numerator). The discrepancy between the CTEQ and MRST01 asymmetry predictions at $y = 0$ can be quantitatively understood by considering their different valence PDFs (see Figs. 13, 14 in Sec. 1.4). In fact a measurement of the asymmetry at the LHC will provide new information to constrain these PDFs.

By contrast, the ratio

$$R_{ZW} = Z/(W^+ + W^-),$$

also shown in Figs. 16, 17 and 18, has very small PDF uncertainties (both experimental and model) and there is no significant variation between PDF sets. To understand this consider that at LO

$$R_{ZW} = (u\bar{u} + d\bar{d} + c\bar{c} + s\bar{s})/(u\bar{d} + d\bar{u} + c\bar{s} + s\bar{c})$$

(modulo electroweak couplings) and that $\bar{d} \sim \bar{u}$ at low-x [3]. This will be a crucial measurement for our understanding of Standard Model Physics at the LHC.

However, whereas the Z rapidity distribution can be fully reconstructed from its decay leptons, this is not possible for the W rapidity distribution, because the leptonic decay channels which we use to identify the W's have missing neutrinos. Thus we actually measure the W's decay lepton rapidity spectra rather than the W rapidity spectra. Fig. 18 also shows the rapidity spectra for positive and negative leptons from W^+ and W^- decay, the lepton asymmetry,

$$A_l = (l^+ - l^-)/(l^+ + l^-)$$

and the ratio

$$R_{Zl} = Z/(l^+ + l^-)$$

[3]There is some small model dependence from the strange sea fraction accounted for in both HERAPDF0.1 and in CTEQ6.6 PDFs.

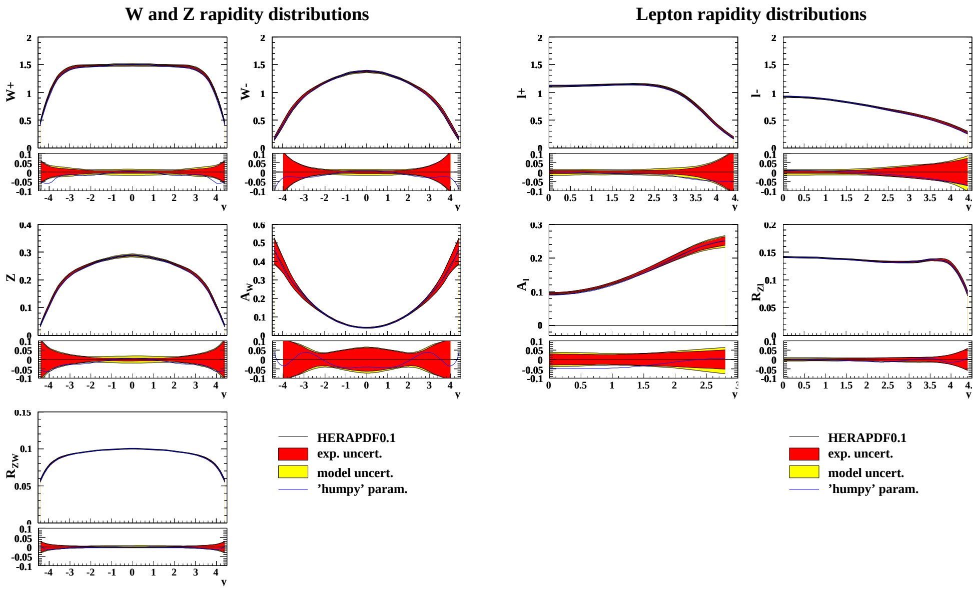

Fig. 18: Left: the W^+, W^-, Z rapidity distributions, A_W, and R_{ZW} (see text) and their experimental uncertainties (red) and model uncertainties (yellow). Right: the l^+, l^- rapidity distributions, A_l and R_{Zl} (see text) and their experimental and model uncertainties. The superimposed blue line represents the results of the alternative 'humpy' gluon parameterization.

A cut of, $p_{tl} > 25$ GeV, has been applied on the decay lepton, since it will not be possible to trigger on leptons with small p_{tl}. A particular lepton rapidity can be fed from a range of W rapidities so that the contributions of partons at different x values is smeared out in the lepton spectra, but the broad features of the W spectra remain.

In summary, these investigations indicate that PDF uncertainties, deriving from experimental error, on predictions for the W, Z rapidity spectra in the central region, have reached a precision of $\sim 1\%$, due to the input of the combined HERA-I data. This level of precision is maintained when using the leptons from the W decay and gives us hope that we could use these processes as luminosity monitors[4]. However, model dependent uncertainties must now be considered very carefully. The current study will be repeated using a general-mass variable-flavour scheme for heavy quarks.

The predicted precision on the ratios R_{ZW}, R_{Zl} is even better since model uncertainties are also very small giving a total uncertainty of $\sim 1\%$. This measurement may be used as a SM benchmark. However the W and lepton asymmetries have larger uncertainties ($5 - 7\%$). A measurement of these quantities would give new information on valence distributions at small-x.

[4] A caveat is that the current study has been performed using PDF sets which are extracted using NLO QCD in the DGLAP formalism. The extension to NNLO gives small corrections $\sim 1\%$. However, there may be much larger uncertainties in the theoretical calculations because the kinematic region involves low-x. There may be a need to account for $ln(1/x)$ resummation or high gluon density effects.

2 Measurements of the Proton Structure Function F_L at HERA [5]

2.1 Introduction

The inclusive deep inelastic ep scattering (DIS) cross section can at low Q^2 be written in terms of the two structure functions, F_2 and F_L, in reduced form as

$$\sigma_r(x, Q^2, y) \equiv \frac{d^2\sigma}{dxdQ^2} \cdot \frac{Q^4 x}{2\pi\alpha^2 Y_+} = F_2(x, Q^2) - \frac{y^2}{Y_+} \cdot F_L(x, Q^2) \,, \tag{4}$$

where $Q^2 = -q^2$ is the negative of the square of the four-momentum transferred between the electron[6] and the proton, and $x = Q^2/2qP$ denotes the Bjorken variable, where P is the four-momentum of the proton. The two variables are related through the inelasticity of the scattering process, $y = Q^2/sx$, where $s = 4E_eE_p$ is the centre-of-mass energy squared determined from the electron and proton beam energies, E_e and E_p. In eq. 4, α denotes the fine structure constant and $Y_+ = 1 + (1-y)^2$.

The two proton structure functions F_2 and F_L are related to the cross sections of the transversely and longitudinally polarised virtual photons interacting with protons, σ_L and σ_T, according to $F_L \propto \sigma_L$ and $F_2 \propto (\sigma_L + \sigma_T)$. Therefore the relation $0 \leq F_L \leq F_2$ holds. In the Quark Parton Model (QPM), F_2 is the sum of the quark and anti-quark x distributions, weighted by the square of the electric quark charges, whereas the value of F_L is zero [14]. The latter follows from the fact that a quark with spin $\frac{1}{2}$ cannot absorb a longitudinally polarised photon.

In Quantum Chromodynamics (QCD), F_L differs from zero, receiving contributions from quarks and from gluons [15]. At low x and in the Q^2 region of deep inelastic scattering the gluon contribution greatly exceeds the quark contribution. Therefore F_L is a direct measure of the gluon distribution to a very good approximation. The gluon distribution is also constrained by the scaling violations of F_2 as described by the DGLAP QCD evolution equations [7–9, 16, 17]. An independent measurement of F_L at HERA, and its comparison with predictions derived from the gluon distribution extracted from the Q^2 evolution of $F_2(x, Q^2)$, thus represents a crucial test on the validity of perturbative QCD (pQCD) at low x. Moreover, depending on the particular theoretical approach adopted, whether it be a fixed order pQCD calculation, a re-summation scheme, or a color dipole ansatz, there appear to be significant differences in the predicted magnitude of F_L at low Q^2. A measurement of F_L may be able to distinguish between these approaches.

Previously the structure function F_L was extracted by the H1 collaboration from inclusive data at high y using indirect methods, as discussed in Sect. 2.2. A preliminary measurement was also presented by the ZEUS collaboration using initial state radiation (ISR) events [18], although the precision of this measurement was limited.

To make a direct measurement of F_L, reduced cross sections must be measured at the same x and Q^2 but with different y values. This can be seen from eq. 4 which states that $F_L(x, Q^2)$ is equal to the partial derivative $\partial\sigma_r(x, Q^2, y)/\partial(y^2/Y_+)$. Due to the relationship $y = Q^2/xs$ this requires data to be collected at different beam-beam centre-of-mass energies, which was done in the last year of HERA running. To maximize the precision of this procedure, the measurable

[5] Contributing authors: J. Grebenyuk, V. Lendermann

[6] The term electron is used here to denote both electrons and positrons unless the charge state is specified explicitly.

range of y^2/Y_+ had to be maximised for each fixed x and Q^2. This was achieved by operating HERA at the lowest attainable centre-of-mass energy and by measuring this data up to the highest possible value of y. An intermediate HERA centre-of-mass energy was also chosen, to improve the precision of F_L extraction and to act as a consistency check. More specifically, between March and June 2007, HERA was operated with proton beam energies, $E_p = 460$ GeV and 575 GeV, compared to the previous nominal value of 920 GeV. The electron beam energy was unaltered at $E_e = 27.6$ GeV. Thus, three data sets, referred to the high- (HER), middle- (MER) and low-energy running (LER) samples, were collected with $\sqrt{s} = 318$ GeV, 251 GeV and 225 GeV, respectively. The integrated luminosities of the data sets used by ZEUS (H1) to measure F_L are 32.8 (21.6) pb^{-1} for HER, 6 (6.2) pb^{-1} for MER and 14 (12.4) pb^{-1} for LER. The specific issues of the recent H1 and ZEUS analyses are discussed in Sect. 2.3, and the results are presented in Sect. 2.4.

2.2 Indirect F_L Extraction by H1

H1 extracted F_L from inclusive data using several indirect methods, which exploit the turn over of the reduced cross section at high y due to the F_L contribution. The basic principle is the following. First, the reduced neutral current cross section σ_r is measured in a y range, where the F_L contribution is negligible and thus the relation $\sigma_r = F_2$ holds very well. Afterward, based on some theoretical assumption, the knowledge of F_2 is extrapolated towards high y. Finally F_L is extracted from the difference between the prediction for F_2 and the measurement of σ_r at high y.

In the analyses at $Q^2 \gtrsim 10\,\mathrm{GeV}^2$ [4, 19, 20] the "extrapolation" method is used. In this method, an NLO QCD PDF fit to H1 HERA I data is performed at $y < 0.35$, and the results are extrapolated to higher y using the DGLAP evolution equations. F_L is then extracted at a fixed $y = 0.75$ and at Q^2 up to 700 GeV^2 using eq. 4. The extracted values are shown in Fig. 19 for the high-Q^2 analysis [4].

At low Q^2, extrapolations of DGLAP fits become uncertain. For $Q^2 \lesssim 2\,\mathrm{GeV}^2$, as the strong coupling constant $\alpha_s(Q^2)$ increases, the higher order corrections to the perturbative expansion become large and lead to the breakdown of the pQCD calculations. Therefore other methods are used in the H1 low-Q^2 data analyses.

The "shape method", as used in the last H1 low-Q^2 study of HERA I data [21], exploits the shape of σ_r in a given Q^2 bin. The Q^2 dependence at high y is driven by the kinematic factor y^2/Y_+ (eq. 4), and to a lesser extent by $F_L(x, Q^2)$. On the other hand, the gluon dominance at low x suggests that F_L may exhibit an x dependence similar to F_2. Therefore it is assumed that F_L is proportional to F_2 and the coefficient of proportionality depends only on Q^2. In the extraction procedure one uses the ratio R of the cross sections of the transversely and longitudinally polarised photons

$$R = \frac{\sigma_T}{\sigma_L} = \frac{F_L}{F_2 - F_L} \tag{5}$$

which is thus assumed to depend only on Q^2. The reduced cross section is fitted by

$$\sigma_r = F_2 \left[1 - \frac{y^2}{Y_+} \frac{R(Q^2)}{1 + R(Q^2)} \right] , \tag{6}$$

where some phenomenological model for F_2 is chosen.

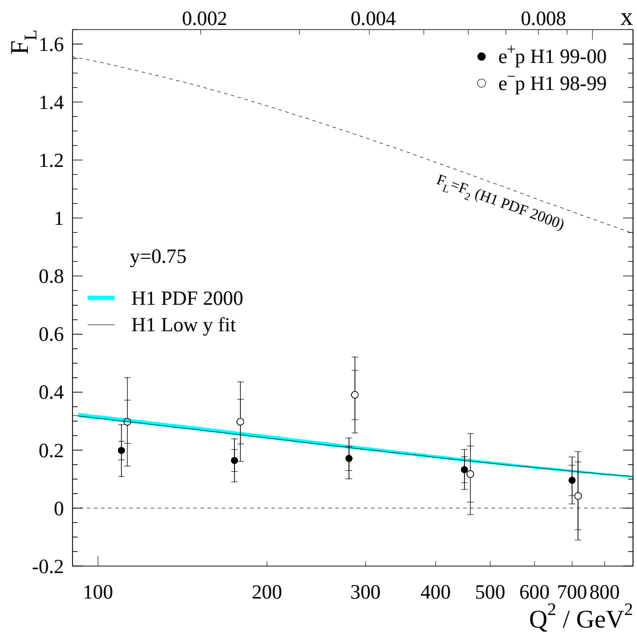

Fig. 19: F_L determined indirectly by H1 at a fixed $y = 0.75$ and high Q^2 is shown as a function of Q^2 (lower scale) or equivalently x (upper scale) for e^+p (closed circles) and e^-p (open circles) data. The inner error bar represents the statistical error, and the outer error bar also includes the systematic error and the uncertainty arising from the extrapolation of F_2.

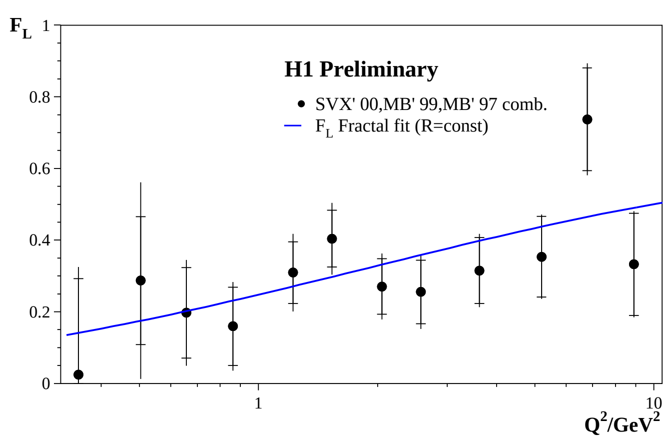

Fig. 20: Q^2 dependence of $F_L(x, Q^2)$ at fixed $y = 0.75$, extracted from the preliminary H1 low-Q^2 data. The solid line shows the prediction of the fractal fit with a constant R.

An example of such an extraction using a fractal fit for F_2 [22] is shown in Fig. 20, where preliminary H1 results [21] for F_L at $y = 0.75$ in the range of $0.35 \leq Q^2 \leq 8.5\,\mathrm{GeV}^2$ are presented. The data favour a positive, not small F_L at low Q^2. A drawback of this method is that it reveals a considerable dependence of R on the choice of the F_2 model.

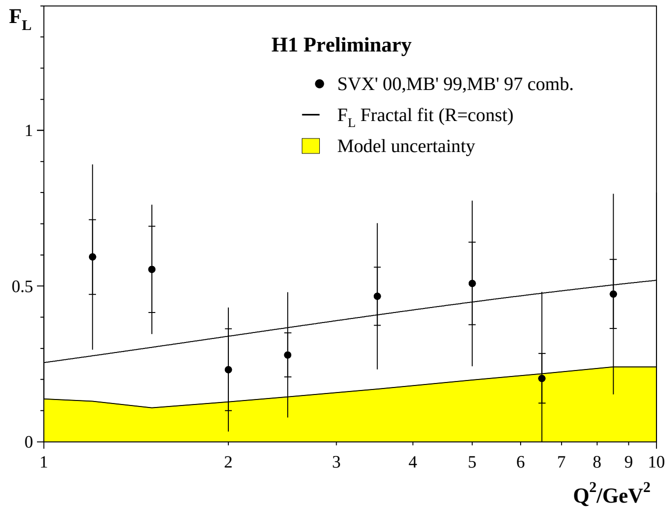

Fig. 21: Structure function F_L extracted by H1 using the derivative method. The solid line shows the prediction of the fractal fit with a constant R. The inner error bars represent statistical uncertainties, the outer error bars represent statistical and systematic uncertainties added in quadrature. The solid (yellow) band indicates the model uncertainty.

In the derivative method [20,21], F_L is extracted from the partial derivative of the reduced cross section on y at fixed Q^2

$$\left.\frac{\partial \sigma_r}{\partial \ln y}\right|_{Q^2} = -x\frac{\partial F_2}{\partial x} - \frac{2y^2(2-y)}{Y_+^2}F_L - x\frac{y^2}{Y_+}\frac{\partial F_L}{\partial x} \tag{7}$$

which is dominated by the F_L-dependent term at high y. The term proportional to $\partial F_L/\partial x$ is negligible for moderately varying parametrisations of F_L. For low Q^2 values the rise of F_2 is weak. The change of the term $x\partial F_2/\partial x$ for the two assumptions: no rise at low x, i.e. $\partial F_2/\partial x = 0$, and $F_2 \propto x^{-\lambda}$ is numerically significantly smaller than the experimental precision for $\partial\sigma_r/\partial \ln y$. Therefore the derivative methods provides a means for determining F_L at low Q^2 with minimal phenomenological assumption. On the other hand, the errors obtained with the derivative method turn out to be significantly larger than those from the shape method.

The preliminary results of F_L extraction from H1 HERA I data [21] are presented in Fig. 21. The residual dependence of the measurement on the assumption made for F_2 is estimated by a comparison with results obtained assuming an F_2 which is flat in y. The lower bound on F_L obtained this way is depicted as a solid band in the figure.

2.3 Details of Direct F_L Measurements

The H1 and ZEUS analysis procedures involve a measurement of the inclusive cross section at $y > 0.1$. In this range, the kinematic variables x, y and Q^2 are most accurately reconstructed using the polar angle, θ_e, and the energy, E'_e, of the scattered electron according to

$$y = 1 - \frac{E'_e}{E_e}\sin^2\frac{\theta_e}{2}\ , \quad Q^2 = \frac{{E'_e}^2\sin^2\theta_e}{1-y}\ , \quad x = \frac{Q^2}{ys}\ . \tag{8}$$

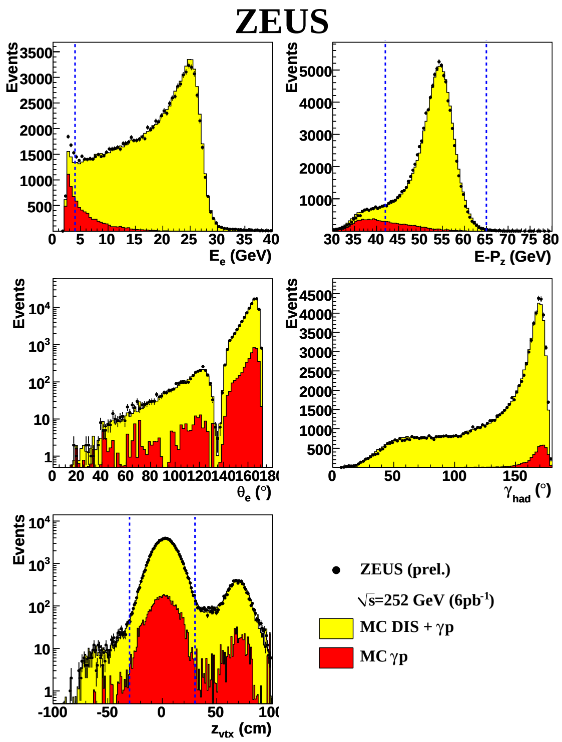

Fig. 22: Comparison of 575 GeV data with the sum of DIS and background simulations for the energy of the scattered electron, total $E - p_z$, theta of the scattered electron, angle of the hadronic final state and z coordinate of the vertex. The dotted lines indicate the cuts applied.

Reaching the high y values necessary for the F_L determination requires a measurement of the scattered electron with energy down to a few GeV. The electron candidate is selected as an isolated electromagnetic energy deposition (cluster) in a calorimeter. The crucial analysis issue at high-y region is the identification of the scattered electron, and the estimation of the hadronic background which occurs when a particle from the hadronic final state mimics the electron signal. Most of background events are photoproduction (γp) events with $Q^2 \approx 0$ in which the final state electron is scattered at low angles (high θ)[7] and thus escapes through the beam pipe.

The γp background suppression is performed in several steps. Firstly, calorimeter shower estimators are utilised which exploit the different profiles of electromagnetic and hadronic showers. Secondly, background coming from neutral particles, such as π_0, can be rejected by requiring a track associated to the electron candidate. Furthermore, γp events are suppressed by utilising the energy-momentum conservation. For that, the variable $E - p_z = \Sigma_i(E_i - p_{z,i})$ is exploited, where the sum runs over energies E_i and longitudinal momentum components $p_{z,i}$ of all particles in the final state. The requirement $E - p_z > 35\,(42)$ GeV in the H1 (ZEUS) analysis removes

[7]The z axis of the right-handed coordinate systems used by H1 and ZEUS is defined by the direction of the incident proton beam with the origin at the nominal *ep* interaction vertex. Consequently, small scattering angles of the final state particles correspond to large polar angles in the coordinate system.

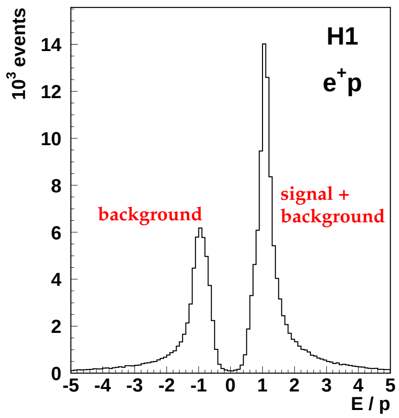

Fig. 23: Distribution of energy over momentum for tracks linked to clusters in the SpaCal with energy from 3.4 to 10 GeV that pass all the medium Q^2 analysis cuts. Tracks with a negative charge are assigned a negative E/p.

events where the escaping electron carries a significant momentum. It also suppresses events with hard initial state photon radiation.

However, at low E_e' the remaining background contribution after such a selection is of a size comparable to or even exceeding the genuine DIS signal. The further analysis steps differ for the H1 and ZEUS analyses as discussed in the following.

ZEUS Analysis Procedure The electron candidates are selected as compact electromagnetic energy depositions in the Uranium Calorimeter (UCal). The position of the candidate is reconstructed using either the Small Angle Rear Tracking Detector (SRTD), which is a high-granularity lead-scintillator calorimeter, or with the Hadron-Electron Separator (HES), which is a silicon detector located in the electromagnetic section of the UCal. The candidates are selected such that $E_e' > 6\,\text{GeV}$[8].

The candidates are validated using information from the tracking devices. The acceptance region for ZEUS tracking is limited to polar angles $\theta_e \lesssim 154^\circ$. The tracking detectors do provide some coverage beyond $\theta_e = 154^\circ$, up to $\theta_e \approx 168^\circ$, however the number of tracking layers is too sparse for full track reconstruction. The hit information from the tracking detectors can still be used. To do this, a "road" is created between the measured interaction vertex and the position of the electron candidate in the calorimeter. Hits in the tracking layers along the road are then counted and compared to the maximum possible number of hits. If too few hits are found, the candidate is assumed to be a neutral particle and it is rejected. To ensure the reliability of this method, the scattered electron is required to exit the central drift chamber at a radius $R > 20\,\text{cm}$. Given that $E_e' > 6\,\text{GeV}$, this effectively limits the maximal y to $y < 0.8$ and the minimum Q^2 achievable at low y. In the HES analysis, events are measured down to $y = 0.2$ roughly translating to the Q^2 region, $Q^2 > 24\,\text{GeV}^2$. No background treatment based on the charge of the candidate is performed.

[8]Cut of $E_e' > 4\,\text{GeV}$ is used for the event selection, although the binning for F_L measurement is chosen such that $E_e' > 6\,\text{GeV}$.

The remaining γp background is estimated using Monte Carlo (MC) simulations. In order to minimise the model uncertainty of the γp simulation, a pure photoproduction sample is selected using an electron tagger placed close to the beam pipe about 6 meters away from the interaction point in the rear direction. It tags, with almost perfect efficiency and purity, the scattered electrons in such events which are not identified in the main detector and escape down the beam pipe. Photoproduction MC is verified against and normalised to this sample. The normalisation factor is found to be 1 ± 0.1 for all data sets.

Figure 22 shows, as an example, comparisons of the 575 GeV data with simulated distributions, for the energy of the scattered electron, total $E - p_z$, polar angle of the scattered electron, angle of the hadronic final state and the z coordinate of the interaction vertex. A good description of the data by the simulation is observed. A similar level of agreement was found for both, HER and LER data sets.

A full set of systematic uncertainties is evaluated for the cross section measurements. The largest single contribution comes from the electron energy scale uncertainty, which is known to within $\pm 1\%$ for $E'_e > 10$ GeV, increasing to $\pm 3\%$ at $E'_e = 5$ GeV. Other significant contributions are due to the $\pm$ 10% uncertainty in verifying the Pythia prediction of the γp cross section using the electron tagger. The systematic uncertainty due to the luminosity measurement was reduced by scaling the three cross sections relative to each other. The spread of relative normalisation factor was found to be within the expected level of uncorrelated systematic uncertainty.

H1 Analysis Procedure The H1 measurements of F_L are performed in separate analyses involving different detector components and thus covering different Q^2 ranges. In the high-Q^2 analysis the electron candidate is selected as an isolated electromagnetic energy deposition in the Liquid Argon (LAr) calorimeter which covers the polar angle range $4^\circ < \theta < 153^\circ$. The selected cluster is further validated by a matching track reconstructed in the central tracking device (CT) with an angular acceptance of $15^\circ < \theta < 165^\circ$. In the medium Q^2 analysis the electron candidate is selected in the backward calorimeter SpaCal covering the angular range $153^\circ < \theta < 177.5^\circ$ and is also validated by a CT track. Lower Q^2 values are expected to be accessed in the third analysis, in which the SpaCal cluster is validated by a track in the Backward Silicon Tracker reaching the highest θ. The first measurement of F_L at medium Q^2 is already published [23], and preliminary results of the combined medium-high-Q^2 analysis are available.

The remaining γp background is subtracted on statistical basis. The method of background subtraction relies on the determination of the electric charge of the electron candidate from the curvature of the associated track.

Figure 23 shows the E/p distribution of the scattered electron candidates from e^+p interactions with the energy E measured in the SpaCal and the momentum p of the linked track determined by the CT. The good momentum resolution leads to a clear distinction between the negative and positive charge distributions. The smaller peak corresponds to tracks with negative charge and thus represents almost pure background. These tracks are termed wrong sign tracks and events with such candidates are rejected. The higher peak, due to right sign tracks, contains the genuine DIS signal superimposed on the remaining positive background. The size of the latter to first approximation equals the wrong sign background. The principal method of background

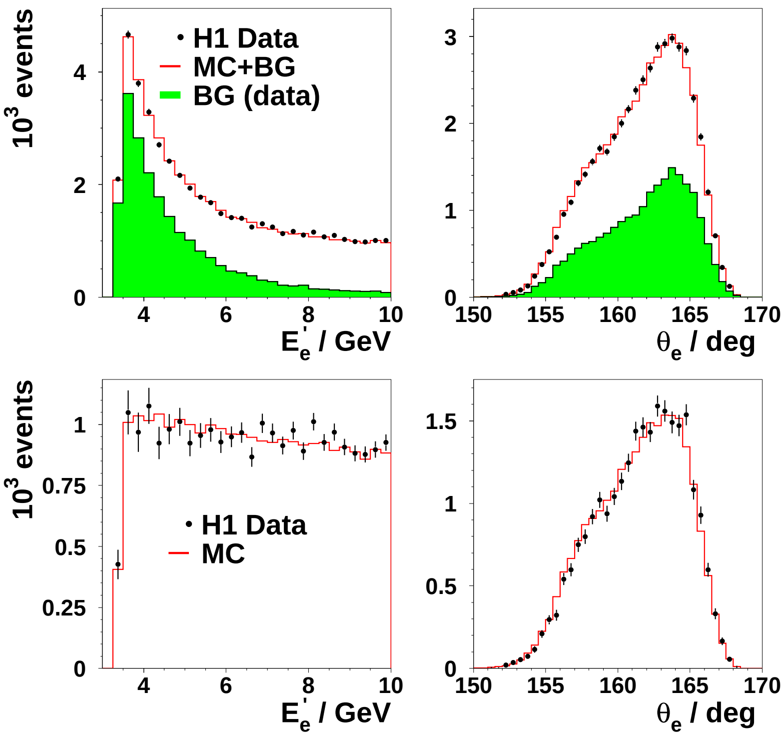

Fig. 24: Top: comparison of the correct sign data (points) with the sum (open histogram) of the DIS MC simulation and background, determined from the wrong sign data (shadowed histogram), for the energy E_e' (left) and the polar angle θ_e (right) of the scattered electron, for the 460 GeV data with $E_e' < 10$ GeV. Bottom: as top but after background subtraction.

subtraction, and thus of measuring the DIS cross section up to $y \simeq 0.9$, consists of the subtraction of the wrong sign from the right sign event distribution in each x, Q^2 interval.

The background subtraction based on the charge measurement requires a correction for a small but non-negligible charge asymmetry in the negative and positive background samples, as has been observed previously by H1 [20]. The main cause for this asymmetry lies in the enhanced energy deposited by anti-protons compared to protons at low energies. The most precise measurement of the background charge asymmetry has been obtained from comparisons of samples of negative tracks in e^+p scattering with samples of positive tracks in e^-p scattering. An asymmetry ratio of negative to positive tracks of 1.06 is measured using the high statistics $e^\pm p$ data collected by H1 in 2003-2006. This result is verified using photoproduction events with a scattered electron tagged in a subdetector of the luminosity system.

Figure 24 shows, as an example, comparisons of the 460 GeV high y data with simulated distributions, for the energy and the polar angle of the scattered electron prior to and after subtraction of the background, which is determined using wrong sign data events.

The measurement of F_L as described below relies on an accurate determination of the variation of the cross section for a given x and Q^2 at different beam energies. In order to reduce

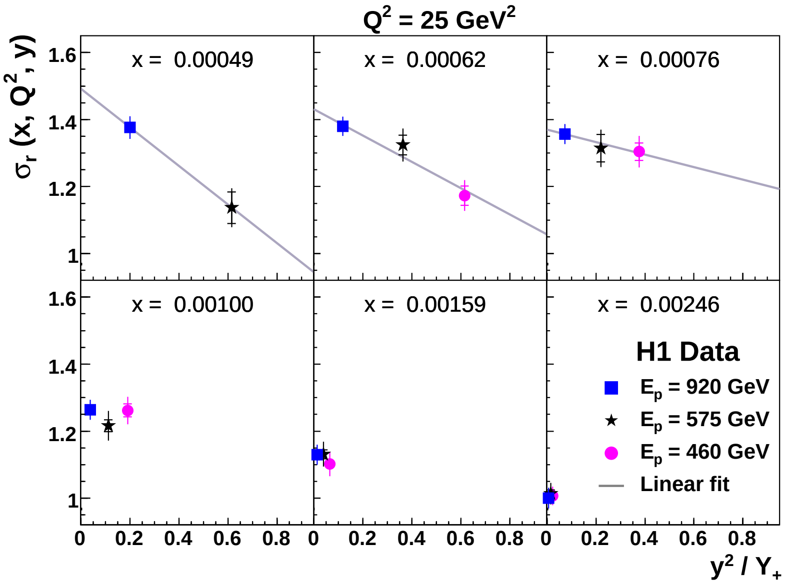

Fig. 25: The reduced inclusive DIS cross section plotted as a function of y^2/Y_+ for six values of x at $Q^2 = 25\,\mathrm{GeV}^2$, measured by H1 for proton beam energies of 920, 575 and 460 GeV. The inner error bars denote the statistical error, the full error bars include the systematic errors. The luminosity uncertainty is not included in the error bars. For the first three bins in x, corresponding to larger y, a straight line fit is shown, the slope of which determines $F_L(x, Q^2)$.

the uncertainty related to the luminosity measurement, which presently is known to 5% for each proton beam energy of the 2007 data, the three data samples are normalised relatively to each other. The renormalisation factors are determined at low y, where the cross section is determined by F_2 only, apart from a small correction due to F_L. The relative normalisation is known to within 1.6%.

All correlated and uncorrelated systematic errors combined with the statistical error lead to an uncertainty on the measured cross sections at high y of 3 to 5%, excluding the common luminosity error.

2.4 Measurements of $F_L(x, Q^2)$ by H1 and ZEUS

The longitudinal structure function is extracted from the measurements of the reduced cross section as the slope of σ_r versus y^2/Y_+, as can be seen in eq. 4. This procedure is illustrated in Fig. 25. The central F_L values are determined in straight-line fits to $\sigma_r(x, Q^2, y)$ as a function of y^2/Y_+ using the statistical and uncorrelated systematic errors.

The first published H1 measurement of $F_L(x, Q^2)$ is shown in Fig. 26, the preliminary ZEUS measurement is presented in Fig. 27. The H1 measured values of F_L are compared with the H1 PDF 2000 fit [4], while the ZEUS F_L values are compared to the ZEUS-JETS PDF fit [3]. Both measurements are consistent and show a non-zero F_L.

The H1 results were further averaged over x at fixed Q^2, as shown in the left panel of Fig. 28. The averaging is performed taking the x dependent correlations between the systematic

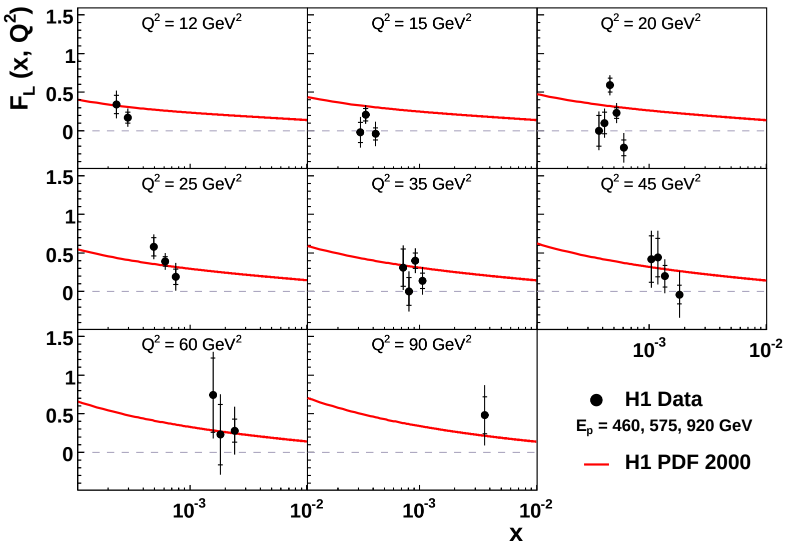

Fig. 26: The longitudinal proton structure function $F_L(x, Q^2)$ measured by the H1 collaboration. The inner error bars denote the statistical error, the full error bars include the systematic errors. The curves represent the H1 PDF 2000 fit.

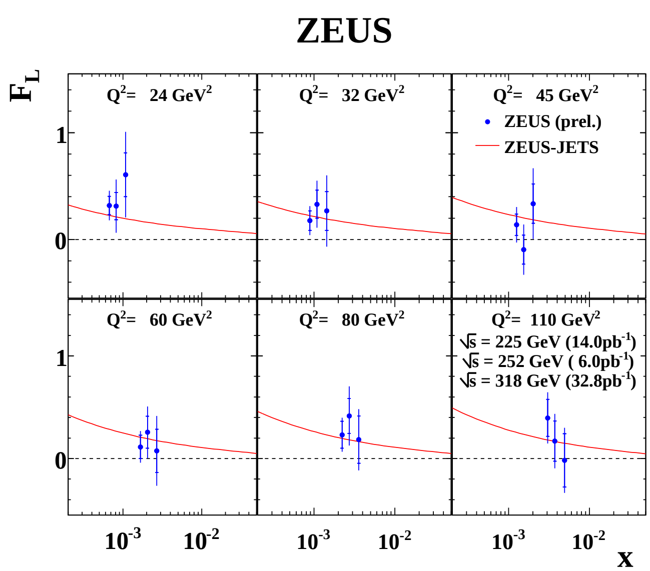

Fig. 27: The longitudinal proton structure function $F_L(x, Q^2)$ measured by the ZEUS collaboration. The inner error bars denote the statistical error, the full error bars include the systematic errors. The curves represent the ZEUS-JETS PDF fit.

errors into account. The averaged values of F_L are compared with H1 PDF 2000 fit and with the expectations from global parton distribution fits at higher order perturbation theory performed by the MSTW [24] and the CTEQ [2, 25] groups. Within the experimental uncertainties the data are consistent with these predictions. The measurement is also consistent with previous indirect

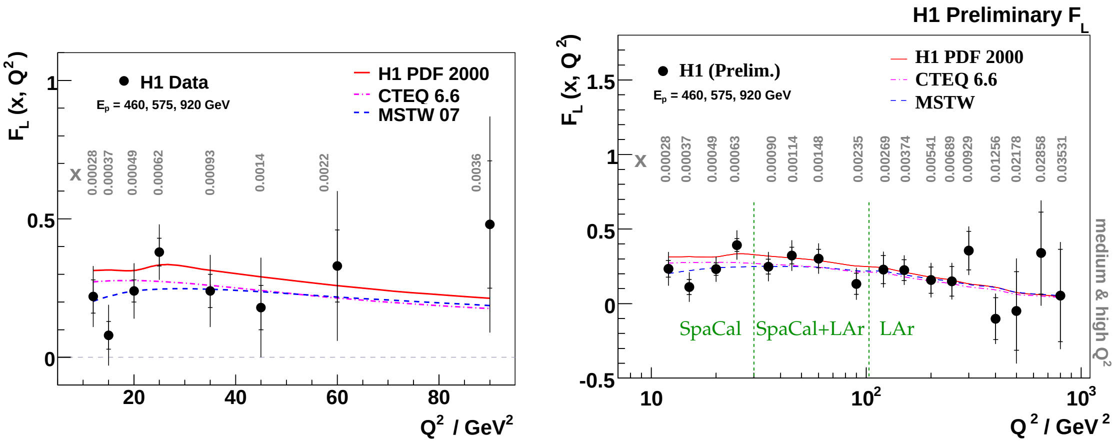

Fig. 28: The proton structure function F_L shown as a function of Q^2 at the given values of x: a) first direct measurement at HERA by H1; b) preliminary H1 results combining SpaCal and LAr analyses. The inner error bars denote the statistical error, the full error bars include the systematic errors. The luminosity uncertainty is not included in the error bars. The solid curve describes the expectation on F_L from the H1 PDF 2000 fit using NLO QCD. The dashed (dashed-dotted) curve depicts the expectation of the MSTW (CTEQ) group using NNLO (NLO) QCD. The theory curves connect predictions at the given (x, Q^2) values by linear extrapolation.

determinations of F_L by H1.

In the combined medium–high Q^2 analysis by H1 the Q^2 range is extended up to $Q^2 = 800\ \mathrm{GeV}^2$. The preliminary results are shown in the right panel of Fig. 28. In some Q^2 bins there is an overlap between the SpaCal and LAr measurements which improves the precision of the F_L extraction as compared to the pure SpaCal analysis.

2.5 Summary

Direct measurements of the proton structure function F_L have been performed in deep inelastic ep scattering at low x at HERA. The F_L values are extracted by the H1 and ZEUS collaborations from the cross sections measured at fixed x and Q^2 but different y values. This is achieved by using data sets collected with three different proton beam energies. The H1 and ZEUS results are consistent with each other and exhibit a non-zero F_L. The measurements are also consistent with the previous indirect determinations of F_L by H1. The results confirm DGLAP NLO and NNLO QCD predictions for $F_L(x, Q^2)$, derived from previous HERA data, which are dominated by a large gluon density at low x.

References

[1] A. M. et al, Eur. Phys.J **C 23**, 73 (2002).

[2] L. L. J. Pumplin, H. and K. T. W. Phys. Rev. **D 75**, 054029 (2007). `hep-ph/0701220`.

[3] ZEUS Collaboration, C. e. a. ZEUS Coll., S. Eur. Phys. J. **C 42**, 1 (2005). `hep-ph/0503274`.

[4] H1 Collaboration, C. Adloff *et al.*, Eur. Phys. J. **C30**, 1 (2003). `hep-ex/0304003`.

[5] A. Cooper-Sarkar, Phys. Rev **D 67**, 012007 (2003).

[6] ZEUS and H. Collaborations, *Combination of h1 and zeus deep inelastic e+- p scattering cross sections*. Preprint ZEUS-prel-07-036, H1prelim-07-007.

[7] L. D. Yu. Sov. Phys. JETP **46**, 641 (1977).

[8] N. G. V. and N. L. L. Sov. J. Nucl. Phys. **15**, 438 (1972).

[9] G. Altarelli and G. Parisi, Nucl. Phys. **B 126**, 298 (1977).

[10] M. Botje, *Qcdnum16.12*. Available from http://www.nikhef.nl/ h24/qcdnum/.

[11] C. Pascaud and F. Zomer, *Qcd analysis from the proton structure function f2 measurement: Issues on fitting, statistical and systematic errors.* Preprint LAL-95-05, 1995.

[12] Particle Data Group Collaboration, C. Amsler *et al.*, Phys. Lett. **B667**, 1 (2008).

[13] M. Dittmar *et al.*, *Parton distributions: Summary report for the HERA - LHC workshop*. Preprint hep-ph/0511119, 2005.

[14] C. Callan and D. Gross, Phys. Rev. Lett. **22**, 156 (1969).

[15] F. W. A. Zee and B. T. S. Phys. Rev. **D 10**, 2881 (1974);
G. Altarelli and G. Martinelli, Phys. Lett. **B 76**, 89 (1978).

[16] N. G. V. and N. L. L. Sov. J. Nucl. Phys. **15**, 675 (1972).

[17] N. L. L. Sov. J. Nucl. Phys. **20**, 94 (1975).

[18] S. C. e. a. ZEUS Coll., in *EPS 2003 conference, Aachen*. 2003.

[19] H1 Collaboration, C. A. e. a. H1 Coll., Phys. Lett. **B 393**, 452 (1997). `hep-ex/9611017`.

[20] H1 Collaboration, C. Adloff *et al.*, Eur. Phys. J. **C21**, 33 (2001). `hep-ex/0012053`.

[21] A. V. Trevino, *Measurement of the Inclusive ep Scattering Cross Section at low Q^2 and x at HERA*, in *Proceedings of the 15th International Workshop on Deep-Inelastic Scattering*. 2007.

[22] T. Lastovicka, Eur. Phys. J. **C 24**, 529 (2002). `hep-ph/0203260`.

[23] H1 Collaboration, D. A. e. a. H1 Coll., F. Phys. Lett. **B 665**, 139 (2008). `0805.2809`.

[24] W. J. S. R. S. T. A. D. Martin and G. Watt, Phys. Lett. **B 652**, 292 (2007). `hep-ph/0706.0459`.

[25] P. M. Nadolsky *et al.*, Phys. Rev. **D78**, 013004 (2008). `0802.0007`.